



---

22 significantly. The influence of earthquake on slope stability is significantly greater than  
23 that of rainfall. The corresponding safety factor when the vertical seismic action is  
24 vertically downward is smaller than that when it is vertically upward. When considering  
25 both horizontal and vertical seismic effects, slope stability is lower.

## 26 **Keywords**

27 Three-dimensional slopes; Rainfall; Earthquake; Stability analysis

## 28 **1 Introduction**

29         Rainfall-induced landslides are caused by the infiltration of precipitation into the  
30 ground surface, leading to an increase in pore water pressure, hence reducing the  
31 effective stress and shear strength of the soil. Sustained rainfall or heavy rainfall events  
32 can significantly increase the risk of slope instability, especially in those areas with  
33 loose, poorly drained soils. Several landslides in the Three Gorges reservoir area have  
34 been triggered by rainfall (Yin et al., 2012; Sun et al., 2016b). Earthquakes, as another  
35 key factor, impose additional dynamic loads on slopes through ground shaking, which  
36 may lead to instability of otherwise stable slopes. In addition, earthquake-induced  
37 landslides tend to be more destructive because they often occur without warning. Due  
38 to completely different destabilization mechanisms, studies of landslides induced by  
39 these two factors are often carried out separately. In some cases, rainfall and  
40 earthquakes may act together on slopes. And earthquake-induced landslides may occur  
41 more frequently during the rainy season, when the soil is saturated with water and its  
42 resistance to earthquakes is reduced. Further research is necessary to investigate the

---

43 stability of slopes under the combined influence of rainfall and earthquake (David, 2000;  
44 Iverson, 2000; Sassa et al., 2010).

45 At present, the main research methods for slope stability include the limit  
46 equilibrium method (Bishop, 1955; Morgenstern and Price, 1965; Spencer, 1967), limit  
47 analysis (Farzaneh et al., 2008; Michalowski, 1995; Qin and Chian, 2018; Zhou et al.,  
48 2017), Finite Element Method (Griffiths and Lane, 1999; Ishii et al., 2012) et al. There  
49 have been numerous studies and findings regarding the stability assessment of 3D  
50 slopes. However, most of these methods are based on extended 3D equilibrium analysis  
51 techniques (Hung, 1987; Zhang, 1988; Chen et al., 2001; Cheng and Yip, 2007), which  
52 rarely strictly adhere to the six equilibrium conditions. Additionally, these approaches  
53 often introduce a significant number of assumptions that limit their practical  
54 engineering applications. The strict 3D limit equilibrium method proposed by Zheng  
55 (2007) is an overall analysis approach based on the natural form of slip surface stress  
56 distribution and approximation through shard interpolation. Sun et al. (2016a, 2017)  
57 combined Morgenstern-Price and Bell global analysis method to analyze the stability  
58 of reservoir bank slope, applying this method to the Three Gorges reservoir area.  
59 Rahardjo et al. (2010) studied the effect of groundwater table position, rainfall  
60 intensities, and soil properties in affecting slope stability using the numerical analyses.  
61 Some of the defects inherent in the two-dimensional(2D) limit equilibrium method  
62 remain unresolved, and some of them are even amplified in the complex 3D analysis,  
63 which has a certain impact on the accuracy of the 3D slope stability evaluation. For the

---

64 limit analysis method, it is still difficult to establish the velocity field of the motion  
65 permit in 3D space. And numerical methods often suffer from two problems: the  
66 determination criteria of the critical state of the slope and the determination of the  
67 location of the critical sliding surface. Compared with a single traditional analysis  
68 method, the mutual integration of several method theories has also been gradually  
69 developed, so as to give full play to the advantages of their respective methods and  
70 better used in slope stability analysis, such as the finite element limit analysis method  
71 (Ali et al., 2017; Lim et al., 2017; Zhou and Qin, 2022).

72 As a common geological hazard in seismic zones, earthquake-triggered landslides  
73 have been extensively investigated by numerous scholars (Sepúlveda et al., 2005;  
74 Chang et al., 2012; Jibson and Harp, 2016; Marc et al., 2017; Salinas-Jasso et al., 2019).  
75 At present, the stability analysis method of 3D slope is not mature, and the research on  
76 the dynamic stability of 3D slope is even more scarce. The quasi-static method (Liu et  
77 al., 2001) introduces coefficients ( $k_v$  and  $k_h$ ) that reflect dynamic action, thereby  
78 transforming a dynamic problem into a static one for easier resolution. This approach  
79 avoids the complexities associated with dynamic analysis and has become widely used  
80 in engineering. Horizontal seismic effects are often a significant consideration in slope  
81 stability analysis, however, some research (Chopra, 1966; Lew, 1991; Ling et al., 1999;  
82 Shukha and Baker, 2008) confirms that the vertical component of seismic forces should  
83 also be given great attention. Wang and Xu (2005) employed the dynamic finite element  
84 method to investigate the seismic response characteristics of various components in a

---

85 3D high slope yet failed to determine the safety factor. Guo et al. (2011) obtained the  
86 time history curve of slope safety factor during earthquake using vector sum method in  
87 2D situations. Cao et al. (2019) studied the seismic response and dynamic failure mode  
88 of the slope subjected to earthquake and rainfall by two model tests. In summary,  
89 although previous researches have provided significant insights into landslides  
90 triggered by earthquakes, there remain inadequacies in fully considering the vertical  
91 effects of seismic activity, extending analysis from 2D to 3D, and comprehensively  
92 integrating the effects of both earthquakes and rainfall.

93 Most studies only consider the role of a single factor in seepage or earthquake,  
94 neglecting the slope stability analysis under combined working conditions. Therefore,  
95 analyzing the change law of safety factors for slopes during seepage and seismic action  
96 is of great practical value in guiding slope support design and evaluating slope stability.  
97 In this paper, a 3D rigorous slice-free method considering seepage and seismic forces  
98 to solve the safety factor of bank slopes is proposed. The proposed method strictly  
99 satisfies the force balance and moment balance in three directions, without introducing  
100 other redundant assumptions.

## 101 **2 Rise of phreatic surface and calculation of seepage force with rainfall** 102 **infiltration in the soil column**

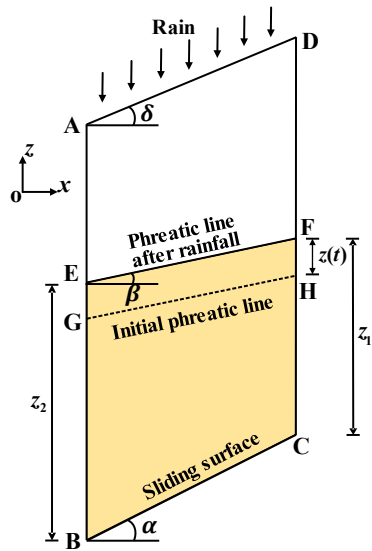
103 The phreatic surface is the interface between the saturated and unsaturated zones  
104 within the slope. Physical and mechanical parameters of the sliding below the phreatic  
105 surface adopt saturated, while above the phreatic surface adopt naturally. A differential

---

106 soil slice is taken from the slip surface to the slope surface in the landslide body is  
 107 shown in Fig. 1.  $z(t)$  is the rise of phreatic surface after rainfall infiltration, which  
 108 refers to Conte et al. (2017), the height of the soil slice below the phreatic line on  $BE$   
 109 and  $CF$  side are respectively  $z_1$  and  $z_2$ . It is assumed that rainfall is consistent with  
 110 groundwater movement and that the slope surface is well drained and free of standing  
 111 water. Regardless of rainfall intensity, runoff will form if it is greater than the infiltration  
 112 capacity. The height of rise of the phreatic surface within the slope after the rainfall is

$$113 \quad z(t) = \frac{z_r}{n(1-S_r)} \exp\left[-\frac{k}{ds \cos \alpha} i \cos \delta (t - t_0)\right] \quad (1)$$

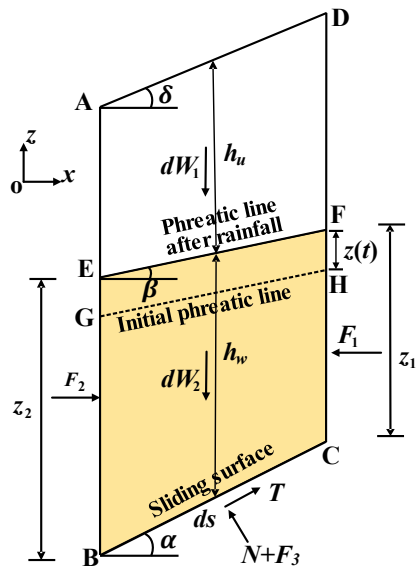
114 where  $z_r$  is the volume of water (per unit area) that infiltrates the slope due to a  
 115 rainfall event with a specified duration,  $n$  is porosity,  $k$  is permeability coefficient,  $S_r$   
 116 is saturation,  $i$  is the hydraulic gradient ( $i = \sin \beta$ ),  $\delta$  is the angle between the slope  
 117 surface and the horizontal plane,  $\alpha$  is the angle between the sliding surface  $BC$  of the  
 118 differential soil slice and the horizontal plane,  $\beta$  is the angle between the phreatic line  
 119 and the horizontal plane,  $ds$  is the length of the sliding surface  $BC$  of the differential  
 120 soil slice,  $t$  is time, and  $t_0$  is the initial moment. As a further simplification, it is  
 121 assumed that both  $n$  and  $S_r$  are constant.



122

123

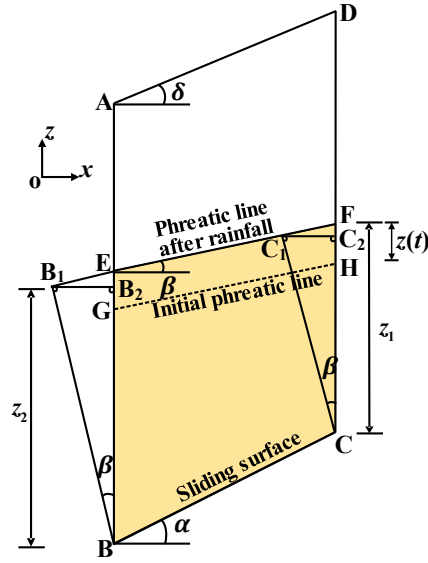
**Fig. 1** Relationship between rainfall and groundwater level



124

125

**Fig. 2** Calculation sketch of forces acting on the differential soil slice



126

127

**Fig. 3** Calculation sketch of hydraulic head

128

The load on the soil slice is shown in Fig. 2.  $dW_1$  and  $dW_2$  are the gravity of the

129

differential soil slice above and below the phreatic line. The resultant hydrostatic force

130

of the boundary  $AB$ ,  $CD$ , and  $BC$  are  $F_1$ ,  $F_2$ , and  $F_3$  respectively.  $N$  is the contact

131

pressure (effective pressure) between the soil particles, and  $T$  is the sliding resistance

132

force.  $h_u$  and  $h_w$  are the height of the soil slice above and below the phreatic line

133

respectively.

134

According to the flow properties of the phreatic line perpendicular to the

135

equipotential line, the surrounding hydrostatic pressures  $F_1$ ,  $F_2$ , and  $F_3$  on the

136

boundary  $CF$ ,  $BE$ , and  $BC$  can be determined. As shown in Fig. 3,  $BB_1$  and  $CC_1$  are

137

perpendicular to the phreatic line, then make  $B_1B_2$  perpendicular to  $AB$ , and  $C_1C_2$

138

perpendicular to  $CD$ . According to the geometric relationship, the hydrostatic pressure

139

resultant forces at the boundary  $CF$  and  $BE$  are

140

$$F_1 = \frac{1}{2} \gamma_w z_1^2 \cos^2 \beta, F_2 = \frac{1}{2} \gamma_w z_2^2 \cos^2 \beta \quad (2)$$



141  $\gamma_w$  is the unit weight of the water. Let  $h_w = \frac{1}{2}(z_1 + z_2)$ , the hydrostatic pressure  
 142 resultant force on the slip surface  $BC$  is

$$143 \quad F_3 = \frac{1}{2} \gamma_w (z_1 + z_2) d s \cos^2 \beta = \gamma_w h_w d s \cos^2 \beta \quad (3)$$

144 The components of  $F_3$  in the horizontal and vertical directions are

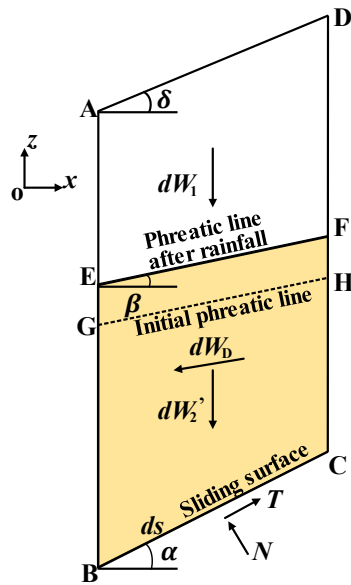
$$145 \quad U_x = \gamma_w h_w d s \cos^2 \beta \cos \alpha, \quad U_y = \gamma_w h_w d s \cos^2 \beta \sin \alpha \quad (4)$$

146 The gravity of water in differential soil slice is

$$147 \quad dW_{2w} = \gamma_w h_w ds \cos \alpha \quad (5)$$

148 The permeability pressure is a pair of balancing forces with the water weight in a  
 149 differential soil slice and the hydrostatic pressure around it (Zheng et al., 2004).

150 Therefore, the weight of water in the differential soil slice and the surrounding  
 151 hydrostatic pressure can be replaced by a seepage force. The force diagram in Fig. 2  
 152 can be replaced by Fig. 4.  $dW'_2$  represents the effective unit weight of the soil below  
 153 the phreatic line and  $dW_D$  is the seepage force.



154

155 **Fig. 4** Simplified force diagram on a differential soil slice

156 The horizontal and vertical component of the seepage force  $dW_3$  are

$$157 \quad dW_{Dx} = F_1 - F_2 + U_x = \gamma_w h_w \cos^2 \beta (z_1 - z_2 + dssin\alpha) \quad (6)$$

$$158 \quad dW_{Dy} = dW_{2w} - U_y = \gamma_w h_w dscos\alpha \sin^2 \beta \quad (7)$$

159 According to geometric relation

$$160 \quad z_1 - z_2 + dssin\alpha = dscos\alpha \tan \beta \quad (8)$$

161 Therefore, the seepage force is

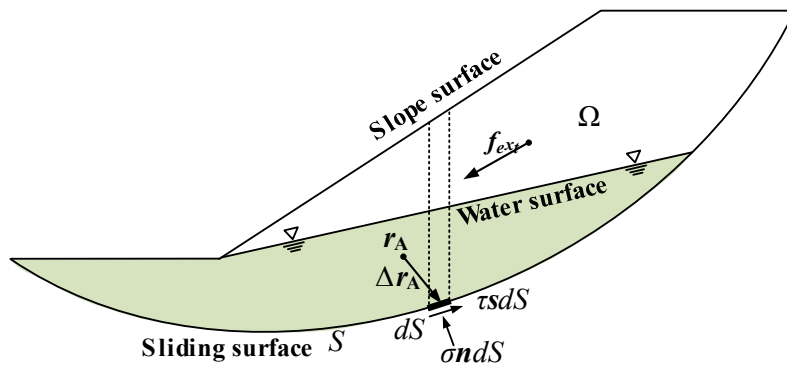
$$162 \quad dW_D = \gamma_w h_w dscos\alpha \sin \beta \quad (9)$$

163 The direction of seepage force is consistent with groundwater flow. The direction  
 164 of groundwater flow within the sliding soil mass is determined by the inclination of the  
 165 phreatic surface in each differential soil slice. As shown in Fig. 4, the flow direction of  
 166 groundwater is oriented at an angle  $\beta$  relative to the horizontal plane.

### 167 **3 A global analysis method for slope stability under seepage and** 168 **earthquake**

#### 169 **3.1 Overall system of equilibrium equations**

170 As shown in Fig. 5, taking the whole sliding body  $\Omega$  as the research object, and  
 171  $S$  is a potential slip surface.



172

173 **Fig. 5** A 2D schematic plot for force system in/on the sliding body

174  $dS$  is a differential element on the sliding surface  $S$ . The normal force on a  
 175 differential element  $dS$  at point  $\mathbf{r}$  is  $\sigma \mathbf{n} dS$ , the resultant shear force is  $\tau s dS$ ,  $\mathbf{n}$  is  
 176 the unit normal vector at position vector  $\mathbf{r}$  on  $S$  and pointing to the inside of the sliding  
 177 body  $\Omega$ ;  $\mathbf{s}$  is the unit tangent vector at position vector  $\mathbf{r}$  on  $S$  and opposed to the  
 178 sliding direction of the sliding body  $\Omega$ , so the reaction on  $dS$  is:

$$179 \quad d\mathbf{f} = (\sigma \mathbf{n} + \tau \mathbf{s}) dS \quad (10)$$

$$180 \quad d\mathbf{m}_A = \Delta \mathbf{r}_A \times d\mathbf{f} \quad (11)$$

181 Here,  $\Delta \mathbf{r}_A = \mathbf{r} - \mathbf{r}_A$ ,  $\mathbf{r}$  is the position vector of  $dS$ ,  $\mathbf{r}_A$  is the position vector for any  
 182 given reference point  $A$ , “ $\times$ ” represents vector multiplication.

183  $\mathbf{f}_{ext}$  is the resultant external force vector, including external loads such as gravity,  
 184 seepage force, seismic force, et al.;  $\mathbf{m}_{ext}$  denotes the moment  $\mathbf{f}_{ext}$  concerning  $\mathbf{r}_A$ . To  
 185 integrate over the entire sliding surface  $dS$ :

$$186 \quad \iint_S d\mathbf{f} + \mathbf{f}_{ext} = \mathbf{0} \quad (12)$$

$$187 \quad \iint_S d\mathbf{m}_A + \mathbf{m}_{ext} = \mathbf{0} \quad (13)$$

188 According to Mohr-Coulomb criterion,

$$189 \quad \tau = \frac{1}{F_s} [c' + f'(\sigma - u)] = \frac{1}{F_s} (c_w + f' \sigma) \quad (14)$$

190 Here,  $F_s$  is the safety factor,  $c'$  and  $f'$  are the effective stress shear strength  
 191 parameters,  $c'$  is cohesion,  $f'$  corresponds to the tangent of the friction angle,  $u$  is  
 192 the pore pressure;  $c_w$  is defined as

$$193 \quad c_w \equiv c' - f' u \quad (15)$$

194 Order,

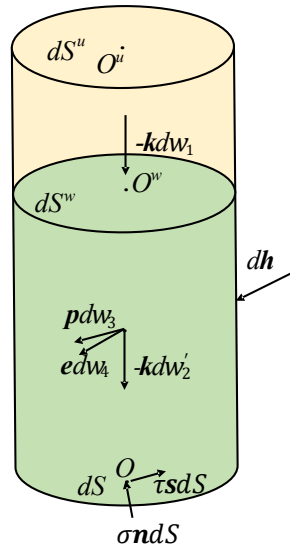
195 
$$\mathbf{n}' = \begin{pmatrix} \mathbf{n} \\ \Delta \mathbf{r}_A \times \mathbf{n} \end{pmatrix}, \quad \mathbf{s}' = \begin{pmatrix} \mathbf{s} \\ \Delta \mathbf{r}_A \times \mathbf{s} \end{pmatrix}, \quad \mathbf{f}_m = \begin{pmatrix} \mathbf{f}_{ext} \\ \mathbf{m}_{ext} \end{pmatrix} \quad (16)$$

196 Substituting equations (10), (11), and (14) into equations (12) and (13), and  
 197 merging into a more compact form:

198 
$$F_s \left( \iint_s \mathbf{n}' \sigma dS + \mathbf{f}_m \right) + \iint_s (c_w + f' \sigma) \mathbf{s}' dS = 0 \quad (17)$$

199 **3.2 Normal stress expression of slip surface under seepage force and seismic force**

200 As shown with the dash line in Fig. 5, a vertical differential cylinder is now taken  
 201 from the homogeneous sliding body from the slip surface to the slope surface. The load  
 202 on the differential cylinder is shown in Fig. 6.  $-kdw_1$  is the weight of the soil above  
 203 phreatic surface, and  $-kdw_2$  refer to the floating weight of the soil below the phreatic  
 204 surface.  $pdw_3$  and  $edw_4$  denote the seepage force and seismic force.  $dh$  refers to the  
 205 action force of the soil around the differential cylinder.



206  
 207 **Fig. 6** Sketch of force acting on a vertical differential cylinder in a sliding body

208 Here,  $\mathbf{k}$  = unit vector of  $z$ -axis;  $\mathbf{p}$  = unit vector pointing to the direction of the  
 209 seepage force;  $\mathbf{e}$  = unit vector pointing to the direction of the seismic force;  $\theta$  = angle

210 between  $dS$  and the horizontal plane;  $\xi$  = angle between the phreatic surface  $dS^w$  and  
 211 the horizontal plane in the differential cylinder.

212 The force equilibrium condition for a differential cylinder is

$$213 \quad \sigma n dS + \tau s dS - k dw_1 - k dw_2' + p dw_3 + e dw_4 + dh = 0 \quad (18)$$

214 Both sides of the Eq. (18) are simultaneously multiplied by  $\mathbf{n}$  to obtain

$$215 \quad \sigma = n_3 \left( \frac{dw_1}{dS} + \frac{dw_1'}{dS} \right) - n_p \frac{dw_3}{dS} - n_e \frac{dw_4}{dS} - \frac{\mathbf{n} \cdot d\mathbf{h}}{dS} \quad (19)$$

216 Here,  $n_3$  = component of  $\mathbf{n}$  in the positive direction of z-axis,  $n_p$  = projection of  
 217  $\mathbf{p}$  in  $\mathbf{n}$  direction,  $n_e$  = projection of  $\mathbf{e}$  in  $\mathbf{n}$  direction.

218 Known,

$$219 \quad \begin{cases} dw_1 = \bar{\gamma} H_u dS \cos \theta \\ dw_2' = \bar{\gamma}' H_w dS \cos \theta \\ dw_3 = \gamma_w H_w dS \cos \theta \sin \xi \\ dw_4 = k_c (\bar{\gamma} H_u + \bar{\gamma}_{sat} H_w) dS \cos \theta \\ n_p = \mathbf{n} \cdot \mathbf{p} \\ n_e = \mathbf{n} \cdot \mathbf{e} \end{cases} \quad (20)$$

220 where,  $\bar{\gamma}$  = average value of the unit weight of the soil above the phreatic surface;  $\bar{\gamma}'$   
 221 = average value for the unit floating weight of the soil below the phreatic surface;  $\bar{\gamma}_{sat}$   
 222 = average value of the unit saturated weight of below the phreatic surface;  $\gamma_w$  = unit  
 223 weight of water;  $H_u$  = height of soil above the phreatic surface;  $H_w$  = height of the soil  
 224 below the phreatic surface;  $k_c$  = seismic force coefficient.

225 Substitute Eq. (20) into Eq. (19) and sort it out

$$226 \quad \sigma = (\bar{\gamma} H_u + \bar{\gamma}' H_w) \cos^2 \theta - n_p \gamma_w H_w \cos \theta \sin \xi - n_e k_c (\bar{\gamma} H_u + \bar{\gamma}_{sat} H_w) \cos \theta - \frac{\mathbf{n} \cdot d\mathbf{h}}{dS} \quad (21)$$

227 Order

---

228 
$$\sigma_0 = (\gamma H_u + \gamma' H_w) \cos^2 \theta - n_p \gamma_w H_w \cos \theta \sin \xi - n_e k_c (\gamma H_u + \gamma_{sat} H_w) \cos \theta,$$

229 
$$h_n = -\frac{\mathbf{n} \cdot d\mathbf{h}}{dS}$$
 (22)

229 Therefore

230 
$$\sigma = \sigma_0 + h_n$$
 (23)

231 Here,  $\sigma_0$  = contribution of volume force to the normal stress.  $h_n$  = contribution  
 232 of the force of surrounding soil to the normal stress of sliding surface.

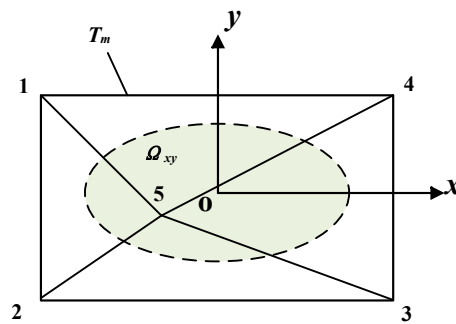
233 The normal stress distribution of the slip surface can be approximated in the  
 234 following (Zheng, 2009):

235 
$$\sigma = \sigma_0 + f(x, y; \mathbf{a})$$
 (24)

236 where  $f(x, y; \mathbf{a})$  = function in the horizontal coordinates  $(x, y)$  with a parametric  
 237 vector  $\mathbf{a}$  consisting of five unknowns.  $f(x, y; \mathbf{a})$  is constructed by piecewise triangular  
 238 linear interpolation:

239 
$$f(x, y; \mathbf{a}) = \mathbf{l}\mathbf{a}$$
 (25)

240 where  $\mathbf{l}$  is the interpolation function,  $\mathbf{l} = (l_1, l_2, \dots, l_5)$ , and it satisfies  $\sum_{i=1}^5 l_i = 1$ .



241

242 **Fig. 7** A triangular mesh for interpolation of normal stress on slip surface

243 As shown in Fig. 7,  $\Omega_{xy}$  is the projection of the sliding body on the  $xoy$  plane, the  
 244 area characterized by the dashed line.  $T_m$  is a triangular network containing 5 nodes.

245  $l_i(x, y) (i = 1, 2, \dots, 5)$  is the interpolation function for these 5 nodes, which can be

---

246 formed as in finite elements with the help of the area coordinates of the 4 triangles on  
247  $T_m$ .

248 Substitute Eq. (24) into Eq. (17), a system of nonlinear equations with  $F_s$  and  $\mathbf{a}$  as  
249 unknowns is obtained:

$$250 \quad F_s \mathbf{B} \mathbf{a} + \mathbf{D} \mathbf{a} + F_s \mathbf{b} + \mathbf{d} = 0 \quad (26)$$

251 Where  $\mathbf{B}$  and  $\mathbf{D}$  are both matrices of order  $6 \times 5$ , and  $\mathbf{b}$  and  $\mathbf{d}$  are both vectors of  
252 order six, whose expressions are respectively.

$$253 \quad \begin{cases} \mathbf{B} = \iint_s \mathbf{n}' l dS \\ \mathbf{D} = \iint_s f' s' l dS \\ \mathbf{b} = \mathbf{f}_m + \iint_s \sigma_0 \mathbf{n}' dS \\ \mathbf{d} = \iint_s (c_w + f' \sigma_0) s' dS \end{cases} \quad (27)$$

254 We can solve Eq. (26) by either Newton's method or eigenvalue method.

255 In Eq. (26), all terms except the resultant external force (moment)  $\mathbf{f}_m$  are area  
256 integrals. The volume integrals on the sliding body involved in the problem are  
257 transformed into boundary integrals that can skip the column partitions. Hence, it is not  
258 required to divide the sliding body into columns anymore, only the surface of the sliding  
259 body needs to be partitioned, as detailed in Zheng (2007).

## 260 **4 Verification examples**

261 In order to verify the accuracy of the proposed method, two examples are analyzed  
262 in this section. Different working conditions were set up for Example 2 and the results  
263 are compared with those calculated by the software.

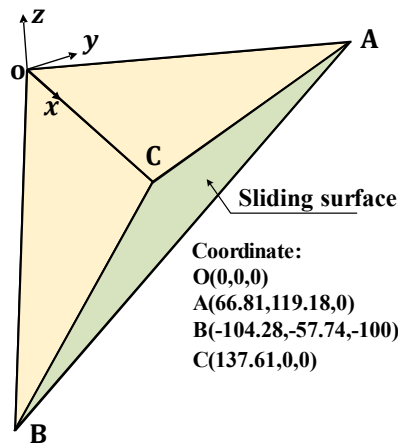
---

#### 264 **4.1 Example 1: translational sliding**

265 Wedge stability in rock mechanics is a typical 3D limit equilibrium analysis  
266 problem. Examples of wedge include two cases of geometric symmetry and asymmetry.  
267 Example 1 is an asymmetric wedge. Fig. 8 shows the three-dimensional model and  
268 geometric parameters of the wedge plane sliding. The sliding surface is composed of  
269 two structural planes, ABC and OAB, and the coordinates of the vertices have been  
270 listed in Fig. 8. The sliding direction of the wedge sliding body is assumed to be parallel  
271 to the intersection line AB. The sliding surface of the wedge adopt the same shear  
272 strength:  $c' = 50\text{kPa}$  and  $\phi' = 30^\circ$ . The unit weight of the wedge is  $26 \text{ kN/m}^3$ . For  
273 simple wedges, the 3D limit equilibrium method has analytical solutions, but these  
274 methods all include an assumption that the shear force on the bottom slip plane is  
275 parallel to the intersecting prism. If the sliding direction of the wedge sliding body is  
276 assumed to be parallel to the intersection line AB of the two structural planes, the wedge  
277 sliding body is statically determinate, and the safety factor has an exact value of 1.640  
278 (Hoek and Bray, 1977) for this example. The safety factor calculated based on the  
279 method in this paper is 1.652. This discrepancy may stem from the triangulation of the  
280 sliding surface. In our method, the sliding surface is approximated using a series of  
281 small triangular elements, which might introduce a slight inaccuracy, leading to a minor  
282 deviation in the calculated safety factor. However, we observed a slight difference  
283 between exact value and the result obtained by the method proposed in our study, it  
284 demonstrates that the proposed method can reasonably evaluate the stability of rocky



285 slopes containing different structural surfaces.



286

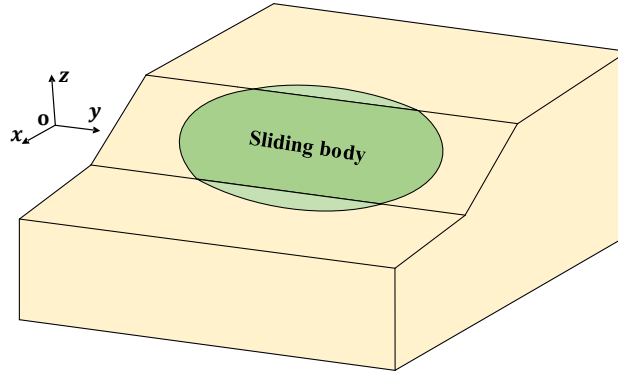
287 **Fig. 8** Model and geometric parameters of the wedge

#### 288 **4.2 Example 2: ellipsoidal sliding**

289 In order to verify the feasibility of the proposed method for calculating the slope  
290 stability under seepage and earthquake, a classical ellipsoid example is selected for the  
291 stability analysis, as shown in Fig.9, which is derived from the study of Zhang (1988).  
292 Zhang's (1988) paper in 1988 provides a three-dimensional slope ellipsoid slip surface  
293 example, and the simplified three-dimensional limit equilibrium method (only three  
294 force equilibrium and one moment equilibrium are satisfied) is used for the stability  
295 analysis. Zhang's (1988) solution for the 3D limit equilibrium of a symmetric ellipsoid  
296 can be regarded as a rigorous solution since the ellipsoid has a symmetric sliding  
297 surface and the other two moment equilibrium conditions are automatically satisfied by  
298 the symmetric bar-column method. Zhang's (1988) solution has also been used by many  
299 scholars to check the correctness of their own procedures (Hung, 1987; Huang and  
300 Tsai, 2000; Zheng, 2009). The example is a homogeneous slope, the potential sliding  
301 surface is a part of a simple ellipsoid, the sliding surface is symmetric about the  $xoz$

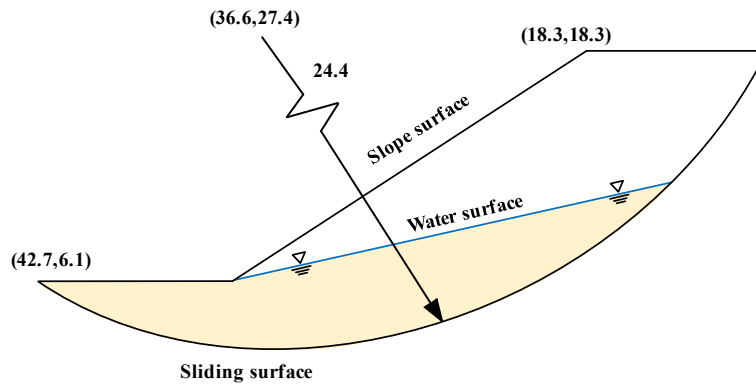
302 plane, and the equation of the sliding surface is

303 
$$\left(\frac{x-36.6}{24.4}\right)^2 + \left(\frac{y}{66.9}\right)^2 + \left(\frac{z-27.4}{24.4}\right)^2 = 1 \quad (26)$$



304

305 **Fig. 9** Model of ellipsoid example



306

307 **Fig. 10** Geometric parameters and middle profile with groundwater

308 The ellipsoid model is shown in Fig. 9. The external load of the slope is only  
 309 considered the effect of gravity, the unit gravity is 19.2kN/m<sup>3</sup>, and the effective shear  
 310 strength parameter:  $c' = 29.3\text{kPa}$  and  $\varphi' = 20^\circ$ . We extended the analysis to include  
 311 complex conditions such as groundwater presence and seismic activity. Four working  
 312 conditions are considered in this section, case-1: no groundwater is considered as in the  
 313 computational model of Zhang (1988); case-2: groundwater is set up as shown in Fig.  
 314 10, the mechanical parameters are listed in Table 1; case-3: earthquake action in the

315 horizontal direction is considered; case-4: both groundwater and horizontal earthquake  
 316 action are considered. Reference to the peak ground acceleration at the location of the  
 317 real slope in the Three Gorges reservoir area in Section 5, the earthquake acceleration  
 318 is taken 0.05g and the horizontal earthquake direction along the x-axis positive direction.  
 319 The results from other methods and our proposed method are listed in Table 2.

320 **Table 1** Mechanical parameters of the slope

Unit weight, $\gamma$ (KN/m <sup>3</sup> )		Shear strength, $c'$ (kPa)		Friction angle, $\phi'$ (°)	
Saturated condition	Unsaturated condition	Saturated condition	Unsaturated condition	Saturated condition	Unsaturated condition
21	19.2	15.8	29.3	13.5	20

321 Case-1: The safety factor calculated using our proposed method is 2.054, whereas  
 322 Zhang (1988) obtained a result of 2.122 using the limit equilibrium method.  
 323 Additionally, we perform a 2D stability analysis of the intermediate cross-section of the  
 324 model using Rocscience's Slide software and obtain a safety factor of 2.084. Comparing  
 325 the results mentioned above, it becomes evident that our proposed method for slope  
 326 stability analysis is feasible, and its calculation results are consistent with the results  
 327 obtained by using the traditional limit equilibrium method and two-dimensional  
 328 stability analysis.

329 Case-2: Only the effect of groundwater seepage is considered. Mechanical  
 330 parameters of the slope below the water surface adopt saturated, while above the water  
 331 surface adopt unsaturated. The groundwater not only induces hydrodynamic effects, but  
 332 also increases the saturation of geotechnical materials, leading to a reduction in soil

---

333 shear strength. In this working condition, the calculated safety factor is 1.183, which is  
334 close to 1.057 calculated by Rocscience's Slide.

335 Case-3: We only consider the effect of horizontal earthquake on slope stability. In  
336 order to compare the results with the 2D stability calculations, we choose the horizontal  
337 seismic action direction to be in the  $xoz$  plane. The results calculated by the 3D  
338 procedure and the 2D software are 1.855 and 1.861, respectively. Compared with the  
339 case-2, the effect of seepage on the slope stability is greater than that of seismic action.

340 Case-4: We considered both seepage and horizontal seismic effects. In this case,  
341 the results calculated by 3D program and 2D software are 1.047 and 0.934 respectively.

342 **Table 2** Safety factor of Example 2

Method	Zhang (1988)	Slide(2D)	The proposed method
Case-1	2.122	2.084	2.054
Case-2	-	1.057	1.183
Case-3	-	1.861	1.855
Case-4	-	0.934	1.047

343 Based on the above calculation results, the comparison revealed minimal  
344 differences across all four conditions (natural, with groundwater, with seismic loading,  
345 and combined), indicating that the proposed method is also effective in assessing slope  
346 stability under seepage and seismic actions.

## 347 **5 A True 3D Slope**

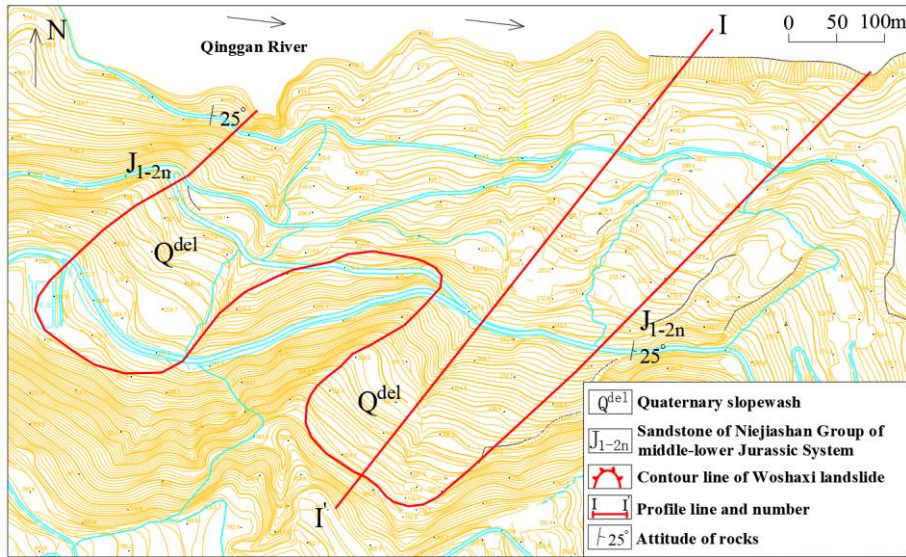
348 This section investigates slope stability evolution under the influence of rainfall  
349 and earthquake by taking an actual slope in the Three Gorges reservoir as a case study.



350

351

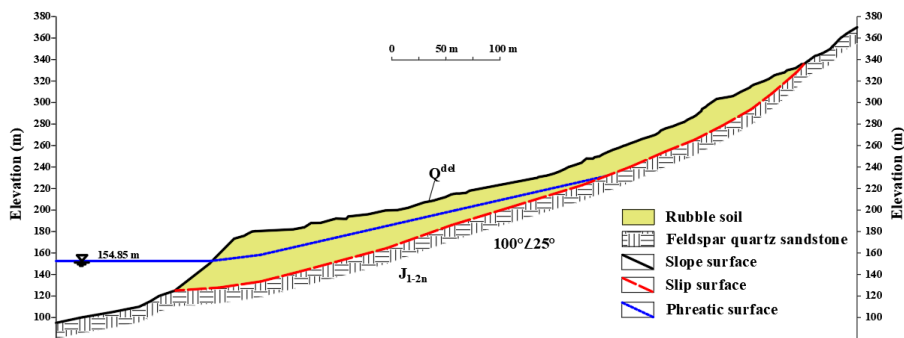
**Fig. 11** Geographical location map of Woshaxi slope (© Google Maps)



352

353

**Fig. 12** Contour map of Woshaxi slope



354

355

**Fig. 13** Geological section map of Woshaxi slope

356

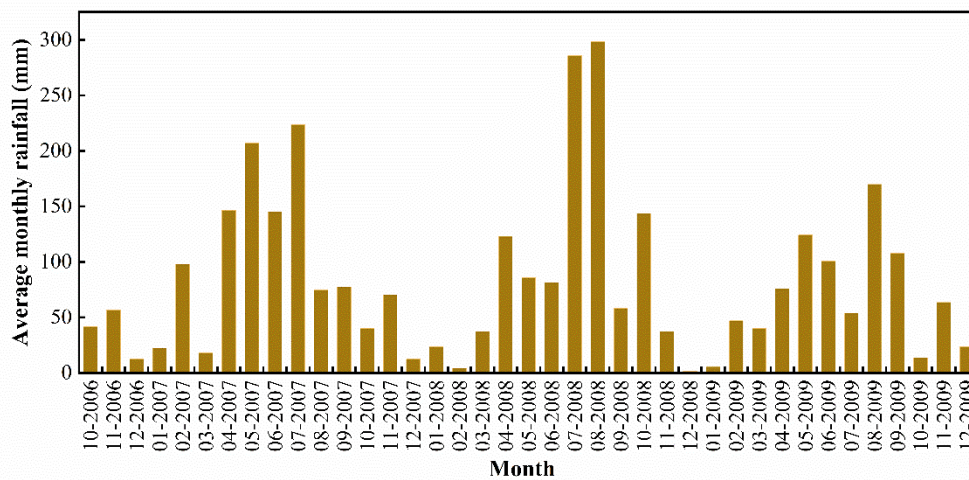
Fig. 11 provides a depiction of the Woshaxi landslide's geographical setting. Fig.

---

357 12 shows a topographic map of Woshaxi slope with contour lines and the cross-section  
358 (I-I') of the landslide is illustrated in Fig. 13. This landslide is located on the right bank  
359 of the Qinggan River, a Yangtze River tributary, and lies about 1.5km away from the  
360 Qianjiangping landslide situated on the river's opposite bank. The composition of the  
361 Woshaxi landslide primarily consists of rubble and soil, underlain by Jurassic-era  
362 sandstone and mudstone layers that are interstratified. The orientation of these rock  
363 layers is  $100^{\circ} \angle 25^{\circ}$ . The landslide has experienced significant impact due to water level  
364 fluctuations in the range of 145-175m, resulting in submersion of its frontal part by  
365 about 20-50m. This geological structure displays a descending gradient from the  
366 southwest to the northeast, with a general gradient of  $20^{\circ}$ . The highest point at the rear  
367 reaching an elevation of 405m, and the front edge descending below 140m. The  
368 landslide encompasses an average thickness of around 15m and a total volume  
369 estimated at  $4.2 \times 10^6 \text{ m}^3$ . Its main sliding direction of the landslide body is toward  $40^{\circ}$   
370 east of north.

371 According to the Seismic Ground Motion Parameter Zonation Map of China, the  
372 peak ground motion acceleration in this region is 0.05g. To investigate slope stability  
373 evolution under seismic conditions, peak accelerations are calculated and analyzed at  
374 various levels. The most dangerous case is considered in the following calculations,  
375 where the direction of the horizontal seismic action coincides with the primary sliding  
376 direction. The precipitation pattern in this region is characterized by relatively  
377 concentrated temporal and spatial distribution. Most of the rainfall occurs between

378 April and October. To investigate the stability of three-dimensional slopes under the  
 379 combined influence of rainfall and earthquake, this study considers the effects of three  
 380 geotechnical parameters: permeability coefficient, porosity, and saturation. The  
 381 proposed method is applied to calculate changes in slope stability resulting from  
 382 average monthly rainfall and earthquake occurring between 2007-2009.



383

**Fig. 14** Average monthly rainfall from 2007 to 2009

384

385 Fig. 14 shows the average monthly rainfall from 2007 to 2009. Table 3 lists the  
 386 physical and mechanical parameters of the landslide body. It is assumed that the  
 387 reservoir water level remains unchanged. To assess the effects of different geotechnical  
 388 parameters and seismic action on the safety factor, four cases are considered: (i) rainfall  
 389 only, (ii) rainfall and horizontal earthquake, (iii) rainfall and vertical earthquake, and  
 390 (iv) rainfall and earthquake in both horizontal and vertical directions.

391

**Table 3** Mechanical parameters of Woshaxi slope

Unit weight, $\gamma$ (KN/m <sup>3</sup> )		Shear strength, $c'$ (kPa)		Friction angle, $\phi'$ (°)	
Saturated condition	Natural condition	Saturated condition	Natural condition	Saturated condition	Natural condition

---

22.4	20.8	18	22	15	20
------	------	----	----	----	----

---

392 (i) Rainfall only

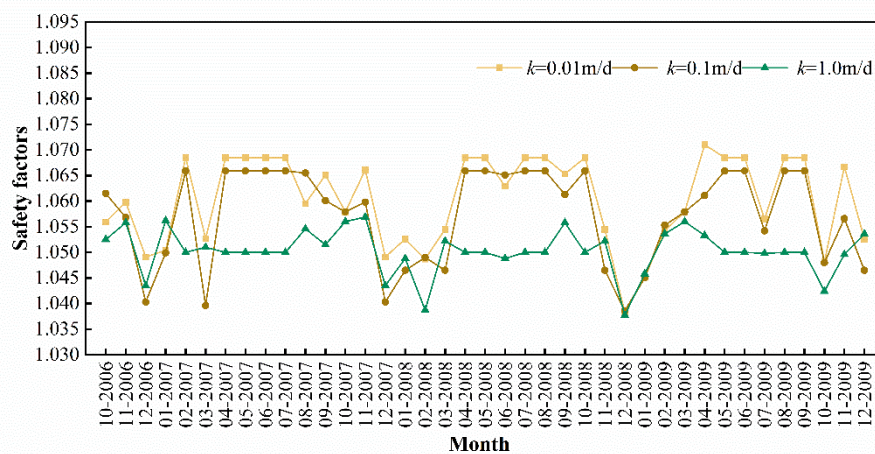
393 The three parameters, infiltration coefficient, porosity, and saturation, have  
394 different effects on the safety factor of slopes. The safety factor varies with the monthly  
395 rainfall. The analysis indicates that an increase in rainfall does not invariably lead to a  
396 decrease in the safety factor of the slope. This phenomenon can be attributed to the fact  
397 that increased rainfall raises the phreatic surface within the slope, affecting two key  
398 aspects: firstly, it enhances the hydrodynamic forces, and secondly, it increases the  
399 pressure at the base of the slope. When the increase in pressure at the slope's base has  
400 a more pronounced impact on stability than the hydrodynamic forces, the safety factor  
401 of the slope will subsequently increase. Conversely, if the hydrodynamic forces  
402 dominate, the stability of the slope will diminish. As shown in Fig. 15(a), the  
403 permeability coefficient  $k$  is 0.01, 0.1 and 1m/d, respectively. With other parameters  
404 unchanged, the trend of safety factor variation for Woshaxi landslide is consistent. The  
405 higher the permeability coefficient, the greater the soil's ability to allow water to pass  
406 through above the phreatic surface, the smaller the rise of the phreatic surface within  
407 the slope. This results in a smaller increase in pressure at the foot of the slope and a  
408 lower safety factor.

409 As shown in Fig. 15(b), the porosity  $n$  is 0.1, 0.3 and 0.5, respectively, and the  
410 safety coefficient of the Woshaxi landslide is consistent under the condition that other  
411 parameters remain unchanged. The higher the porosity, the greater the soil permeability  
412 above the phreatic surface, the smaller the rise of the phreatic surface within the slope,



413 resulting in a smaller increase of pressure at the slope's foot and thus a lower safety  
414 factor.

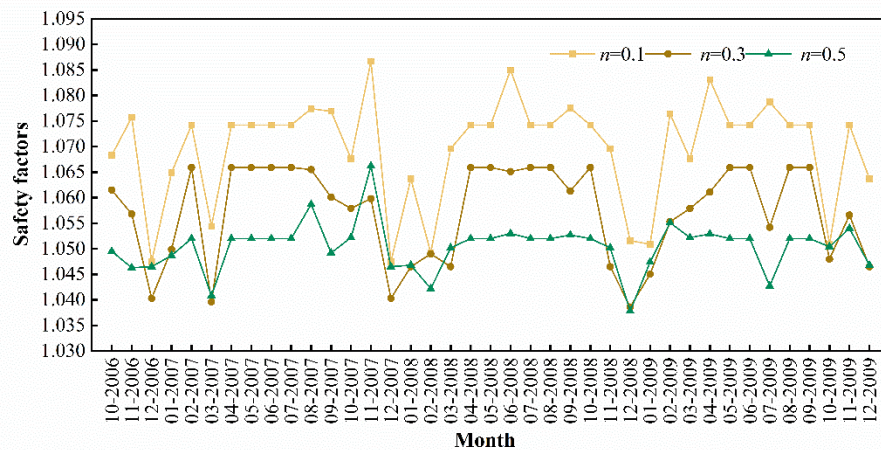
415 As shown in Fig. 15(c), the saturation  $S_r$  of the soil above the phreatic surface of  
416 the landslide is 0.4, 0.6 and 0.8, respectively, and the safety factor of the Woshaxi  
417 landslide is consistent under other parameters remained unchanged. The higher the  
418 saturation, the lower the permeability of soil above the phreatic surface, resulting in a  
419 greater rise of phreatic surface within the slope and an increased pressure at its foot,  
420 thereby leading to a higher safety factor. Overall, under rainfall conditions, soil porosity  
421 on the phreatic surface has a greater impact on safety factor than permeability  
422 coefficient and saturation.



423

424

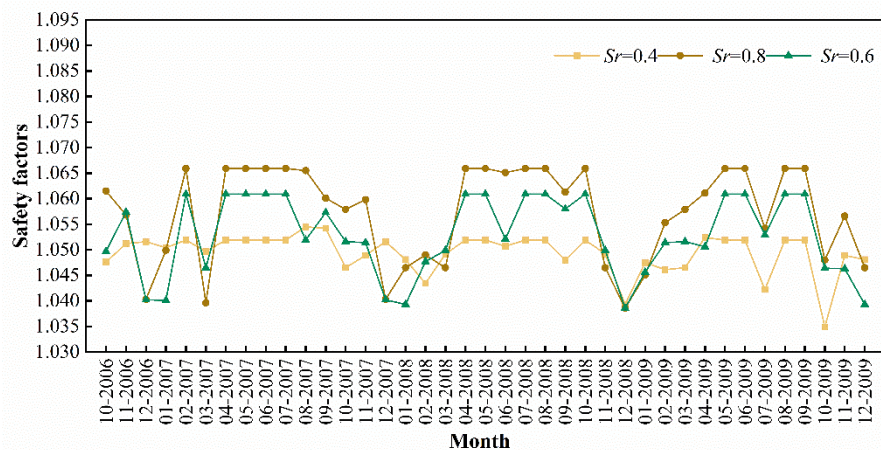
(a) permeability coefficient



425

426

(b) porosity



427

428

(c) saturation

**Fig. 15** Safety factors of the Woshaxi landslide under rainfall

429

430

(ii) Rainfall and horizontal earthquake

431

Fig. 16 shows the evolution of the stability of the Woshaxi landslide under the

432

combined effect of rainfall and horizontal earthquake with different geotechnical

433

parameters, and the horizontal earthquake coefficient  $k_h$  is taken as 0.05. Comparing

434

with Fig. 15, it can be observed that after considering the effect of horizontal earthquake,

435

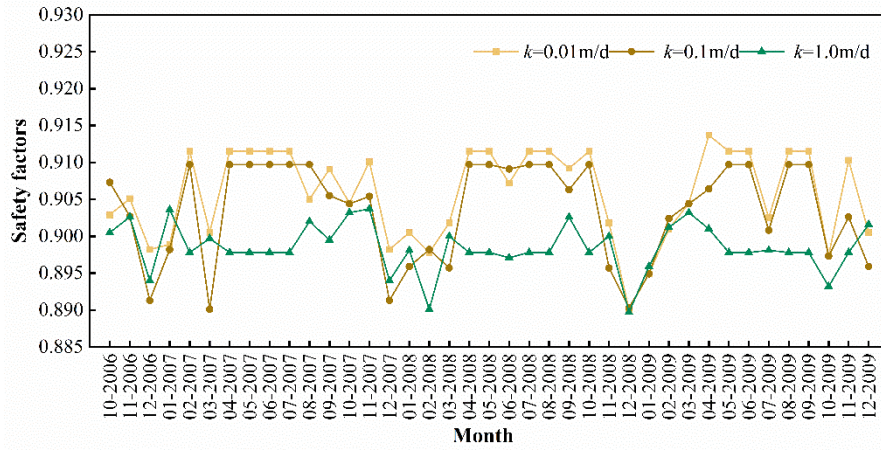
the variation trend of the safety factor of the Woshaxi landslide calculated with different

436

geotechnical parameters is consistent with that under the rainfall condition only, but the

---

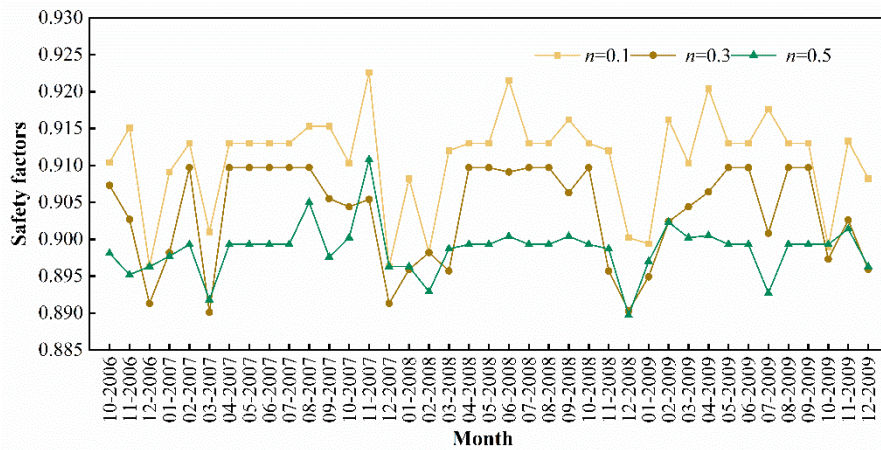
437 stability of the landslide is obviously decreased. Fig. 17 shows the evolution of the  
438 stability of the Woshaxi landslide with rainfall and different horizontal earthquake  
439 coefficients. With other parameters unchanged, the values of the horizontal earthquake  
440 coefficients are 0.05, 0.1 and 0.15 respectively. In this research, we employed three  
441 different horizontal earthquake coefficients: 0.05, 0.1, and 0.15. The coefficient of 0.05  
442 is based on the seismic zoning map of China, corresponding to the seismic  
443 characteristics and expected level of seismic activity in the study area. As for the other  
444 two coefficients, 0.1 and 0.15, they are not directly associated with any specific  
445 earthquake magnitude or return period. These values were set based on engineering  
446 requirements and safety considerations, aiming to assess the variation in slope stability  
447 under stronger seismic actions. This approach allows us to understand the response of  
448 the slope under different seismic intensities and provides a safety margin for seismic  
449 activities that may exceed expectations. Our study has revealed that within the specific  
450 context of the examined landslide, as the horizontal earthquake coefficient increases,  
451 there is a notable decrease in the safety factor. It is also observed that in this particular  
452 case, the impact of seismic activity on slope stability appears to be considerably more  
453 pronounced than that of rainfall. However, these findings are derived from a singular  
454 case study, focusing on a specific landslide morphology and set of soil properties.  
455 Consequently, they may not necessarily be universally applicable across different  
456 landslide types and varying geological conditions.



457

458

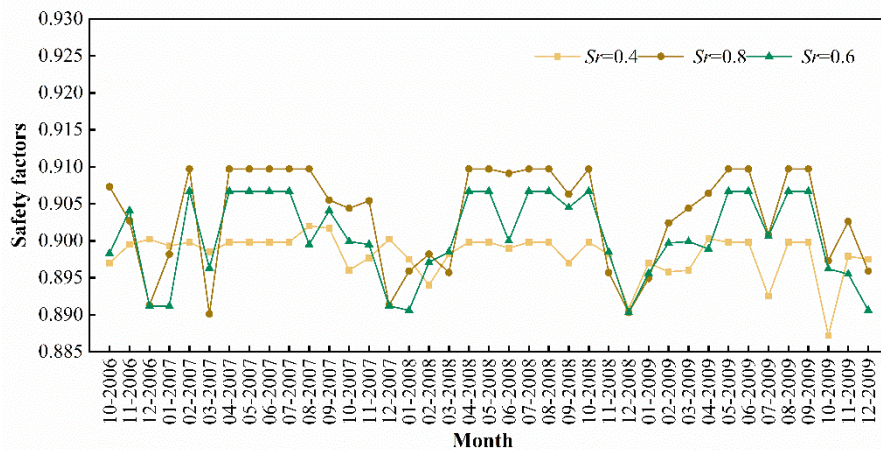
(a) permeability coefficient



459

460

(b) porosity



461

462

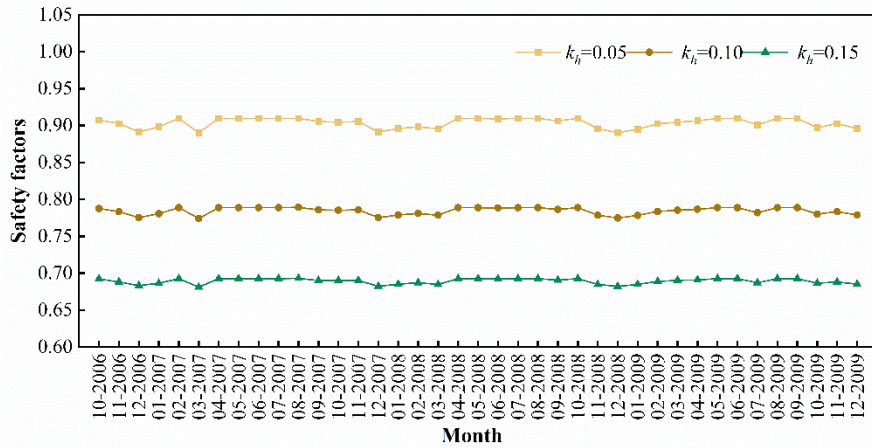
(c) saturation

463

**Fig. 16** Safety factors of the Woshaxi landslide under rainfall and horizontal

464

earthquake ( $k_h = 0.05$ )



465

466 **Fig. 17** Safety factors of the Woshaxi landslide under rainfall and horizontal  
 467 earthquake (different horizontal seismic coefficient)

468 (iii) Rainfall and vertical earthquake

469 Fig. 18 shows the evolution of the stability of the Woshaxi landslide with rainfall

470 and different vertical earthquake coefficients. With other parameters unchanged, the

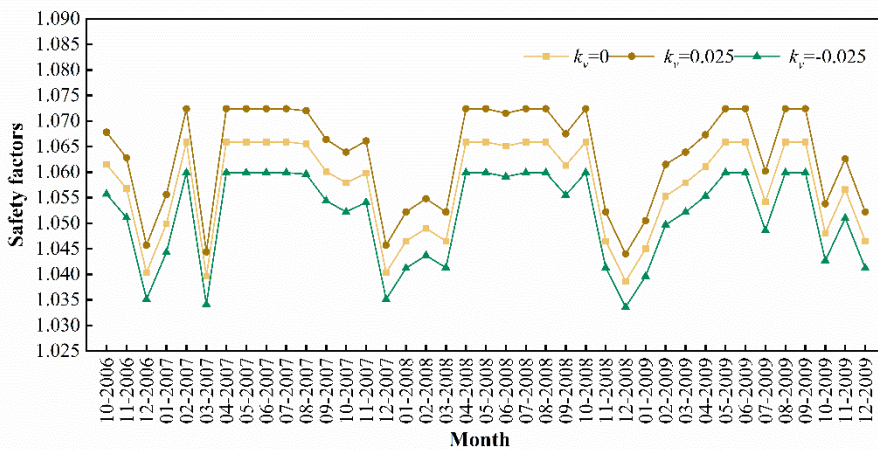
471 vertical earthquake coefficient  $k_v$  takes on values of 0.025, 0, and -0.025 respectively,

472 and the negative sign indicates that the direction of vertical earthquake is vertically

473 downward. It is obvious from Fig. 18 that the corresponding safety factor when the

474 earthquake acts vertically downward is smaller than the corresponding safety factor

475 when it is vertically upward.



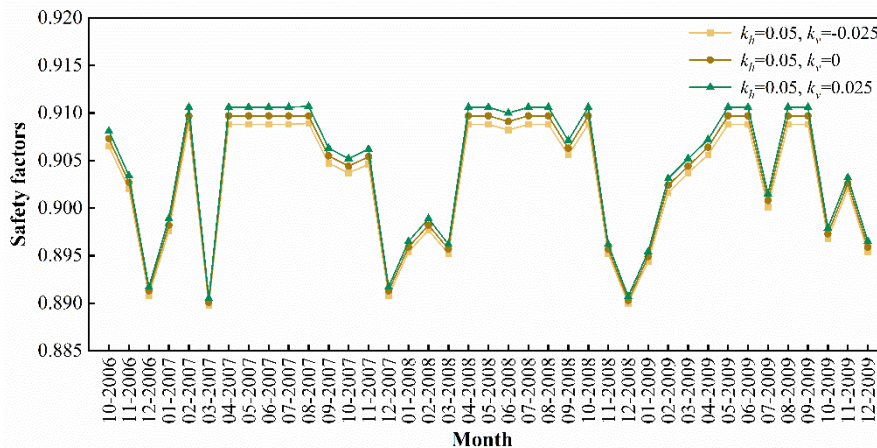
476



477 **Fig. 18** Safety factors of the Woshaxi landslide under rainfall and vertical earthquake

478 (iv) Rainfall and earthquake in both horizontal and vertical directions

479 Fig. 19 shows the evolution of the stability of the Woshaxi landslide with rainfall  
480 and different earthquake coefficients. Horizontal earthquake coefficient  $k_h$  is taken as  
481 0.05, and the values of vertical earthquake coefficient are 0.025, 0, -0.025 respectively,  
482 and the negative sign indicates that the direction of vertical earthquake action is  
483 vertically downward. Under the condition that other parameters remain unchanged, the  
484 slope stability is lower when considering both horizontal and vertical upward  
485 earthquake compared to considering only horizontal earthquake. Therefore, it is  
486 essential to properly account for the effect of vertical earthquake in order to ensure  
487 maximum safety.



488

489 **Fig. 19** Safety factors of the Woshaxi landslide under rainfall and earthquake (in both

490 horizontal and vertical directions)

## 491 6 Conclusions

492 In this paper, the calculation of the seepage force is studied, the normal stress  
493 expression on the sliding surface of a slope under seepage force and seismic force are

---

494 also derived. Furthermore, a global analysis method that considers both seepage and  
495 seismic forces is proposed to determine the safety factor of slopes subjected to the  
496 combined effect of rainfall and earthquake. The reliability of the proposed method is  
497 also verified with two examples combining software calculations and previous results.

498 Taking a slope in the Three Gorges reservoir area as an example, this study  
499 investigates the influence of soil permeability coefficient, porosity and saturation on  
500 slope stability, and analyzes the safety evolution of this slope under combined effects  
501 of rainfall and earthquake. The results indicate that, under rainfall conditions, the  
502 porosity of the soil above the phreatic surface exerts a greater influence on safety factor  
503 than permeability coefficient and saturation. With an increase in the horizontal  
504 earthquake coefficient, the safety factor of the landslide is significantly reduced, and  
505 the impact of earthquake on slope stability surpasses that of rainfall. The safety factor  
506 corresponding to vertical downward earthquake action is smaller than that of vertical  
507 upward, and the stability of slope is lower when considering horizontal and vertical  
508 upward earthquake actions. Therefore, in order to ensure maximum safety, proper  
509 consideration should be given to vertical earthquake actions.

510 When considering rainfall alone, the slope safety factor is 1.04-1.09, positioning  
511 the slope in a state that between unstable and basically stable. However, upon  
512 accounting for horizontal seismic activity, the slope safety factor decreases to about 0.9  
513 and is transformed into an unstable state. When the vertical earthquake is considered,  
514 the slope safety factor is 1.035-1.075. This represents a slight reduction but still in the

---

515 unstable and basically stable state. This suggests that horizontal seismic influences  
516 exert a more pronounced impact on slope stability compared to vertical. When rainfall  
517 and earthquake act simultaneously, the safety factor calculated using the proposed  
518 method falls below 1.0, indicating an unstable condition where landslide disasters are  
519 likely to occur on the slope. The research results provide scientific basis for slope  
520 stability analysis and prevention. Further, the proposed method can identify potential  
521 risk areas for landslide hazards, and planners in the Three Gorges Reservoir area can  
522 better consider these risks and take measures to increase the seismic and flood resilience  
523 of reservoir infrastructure.

#### 524 **Data availability**

525 The data used in this study are available from the first author upon request.

#### 526 **Author contribution**

527 JW analyzed the data, conceived the paper, and wrote the paper; ZW conceived  
528 and co-wrote the paper; HL reviewed and improved the analysis and paper; and GS  
529 provided the data of the actual slope in the Three Gorges reservoir.

#### 530 **Competing interests**

531 The contact author has declared that none of the authors has any competing  
532 interests.

#### 533 **Acknowledgments**

534 This study was supported by the National Natural Science Foundation of China  
535 (Grant No.11972043).



---

536 **References**

- 537 Ali, A., Lyamin, A. V., Huang, J., Li, J. H., Cassidy, M. J., and Sloan, S. W.: Probabilistic  
538 stability assessment using adaptive limit analysis and random fields, *Acta Geotech.*, 12,  
539 937–948, <https://doi.org/10.1007/s11440-016-0505-1>, 2017.
- 540 Bishop, A. W.: The use of the Slip Circle in the Stability Analysis of Slopes,  
541 *Géotechnique*, 5, 7–17, <https://doi.org/10.1680/geot.1955.5.1.7>, 1955.
- 542 Cao, L., Zhang, J., Wang, Z., Liu, F., Liu, Y., and Zhou, Y.: Dynamic response and  
543 dynamic failure mode of the slope subjected to earthquake and rainfall, *Landslides*, 16,  
544 1467–1482, <https://doi.org/10.1007/s10346-019-01179-7>, 2019.
- 545 Chang, K.-T., Lin, M.-L., Dong, J.-J., and Chien, C.-H.: The Hungtsaiping landslides:  
546 from ancient to recent, *Landslides*, 9, 205–214, [https://doi.org/10.1007/s10346-011-](https://doi.org/10.1007/s10346-011-0293-5)  
547 0293-5, 2012.
- 548 Chen Z., Hongliang M. I., and Xiaogang W.: A three-dimensional limit equilibrium  
549 method for slope stability analysis, *ytcxb*, 23, 525–529, 2001.
- 550 Cheng, Y. M. and Yip, C. J.: Three-Dimensional Asymmetrical Slope Stability Analysis  
551 Extension of Bishop’s, Janbu’s, and Morgenstern–Price’s Techniques, *Journal of*  
552 *Geotechnical and Geoenvironmental Engineering*, 133, 1544–1555,  
553 [https://doi.org/10.1061/\(ASCE\)1090-0241\(2007\)133:12\(1544\)](https://doi.org/10.1061/(ASCE)1090-0241(2007)133:12(1544)), 2007.
- 554 Chopra, A. K.: The importance of the vertical component of earthquake motions,  
555 *Bulletin of the Seismological Society of America*, 56, 1163–1175, 1966.
- 556 Conte, E., Donato, A., and Troncone, A.: A simplified method for predicting rainfall-

---

557 induced mobility of active landslides, *Landslides*, 14, 35–45,  
558 <https://doi.org/10.1007/s10346-016-0692-8>, 2017.

559 David, K. K.: Statistical analysis of an earthquake-induced landslide distribution—the  
560 1989 Loma Prieta, California event, *Engineering geology*, 58, 231–249, 2000.

561 Farzaneh, O., Askari, F., and Ganjian, N.: Three-Dimensional Stability Analysis of  
562 Convex Slopes in Plan View, *J. Geotech. Geoenviron. Eng.*, 134, 1192–1200,  
563 [https://doi.org/10.1061/\(ASCE\)1090-0241\(2008\)134:8\(1192\)](https://doi.org/10.1061/(ASCE)1090-0241(2008)134:8(1192)), 2008.

564 Griffiths, D. V. and Lane, P. A.: Slope stability analysis by finite elements,  
565 *Géotechnique*, 49, 387–403, <https://doi.org/10.1680/geot.1999.49.3.387>, 1999.

566 Guo, M., Ge, X., Wang, S., and Wang, H.: Dynamic stability analysis of slope based on  
567 vector sum analysis method, *Chin. J. Rock Mech. Eng.*, 30, 572–579, 2011.

568 Hoek, E. and Bray, J. D.: *Rock Slope Engineering*, The Institute of Mining and  
569 Metallurgy, London, 1977.

570 Huang, C.-C. and Tsai, C.-C.: New Method for 3D and Asymmetrical Slope Stability  
571 Analysis, *J. Geotech. Geoenviron. Eng.*, 126, 917–927,  
572 [https://doi.org/10.1061/\(ASCE\)1090-0241\(2000\)126:10\(917\)](https://doi.org/10.1061/(ASCE)1090-0241(2000)126:10(917)), 2000.

573 Hungr, O.: An extension of Bishop’s simplified method of slope stability analysis to  
574 three dimensions, *Géotechnique*, 37, 113–117,  
575 <https://doi.org/10.1680/geot.1987.37.1.113>, 1987.

576 Ishii, Y., Ota, K., Kuraoka, S., and Tsunaki, R.: Evaluation of slope stability by finite  
577 element method using observed displacement of landslide, *Landslides*, 9, 335–348,

---

578 <https://doi.org/10.1007/s10346-011-0303-7>, 2012.

579 Iverson, R. M.: Landslide triggering by rain infiltration, *Water Resources Research*, 36,  
580 1897–1910, <https://doi.org/10.1029/2000WR900090>, 2000.

581 Jibson, R. W. and Harp, E. L.: Ground motions at the outermost limits of seismically  
582 triggered landslides, *Bulletin of the Seismological Society of America*, 106, 708–719,  
583 2016.

584 Lew, M.: Characteristics of Vertical Ground Motions Recorded During the Lorna Prieta  
585 Earthquake, 1991.

586 Lim, K., Li, A. J., Schmid, A., and Lyamin, A. V.: Slope-Stability Assessments Using  
587 Finite-Element Limit-Analysis Methods, *Int. J. Geomech.*, 17, 06016017,  
588 [https://doi.org/10.1061/\(ASCE\)GM.1943-5622.0000715](https://doi.org/10.1061/(ASCE)GM.1943-5622.0000715), 2017.

589 Ling, H. I., Mohri, Y., and Kawabata, T.: Seismic analysis of sliding wedge: extended  
590 Francais–Culmann’s analysis, *Soil Dynamics and Earthquake Engineering*, 18, 387–  
591 393, 1999.

592 Liu, L. P., Lei, Z. Y., and Zhou, F. C.: The evaluation of seismic slope stability analysis  
593 methods, *Journal of Chongqing Jiaotong University*, 20, 83–88, 2001.

594 Marc, O., Meunier, P., and Hovius, N.: Prediction of the area affected by earthquake-  
595 induced landsliding based on seismological parameters, *Natural Hazards and Earth  
596 System Sciences*, 17, 1159–1175, 2017.

597 Michalowski, R. L.: Slope stability analysis: a kinematical approach, *Géotechnique*, 45,  
598 283–293, <https://doi.org/10.1680/geot.1995.45.2.283>, 1995.

---

599 Morgenstern, N. R. and Price, V. E.: The Analysis of the Stability of General Slip  
600 Surfaces, *Géotechnique*, 15, 79–93, <https://doi.org/10.1680/geot.1965.15.1.79>, 1965.

601 Qin, C.-B. and Chian, S. C.: Kinematic analysis of seismic slope stability with a  
602 discretisation technique and pseudo-dynamic approach: a new perspective,  
603 *Géotechnique*, 68, 492–503, <https://doi.org/10.1680/jgeot.16.P.200>, 2018.

604 Rahardjo, H., Nio, A. S., Leong, E. C., and Song, N. Y.: Effects of Groundwater Table  
605 Position and Soil Properties on Stability of Slope during Rainfall, *J. Geotech.*  
606 *Geoenviron. Eng.*, 136, 1555–1564, [https://doi.org/10.1061/\(ASCE\)GT.1943-](https://doi.org/10.1061/(ASCE)GT.1943-5606.0000385)  
607 [5606.0000385](https://doi.org/10.1061/(ASCE)GT.1943-5606.0000385), 2010.

608 Salinas-Jasso, J. A., Ramos-Zuñiga, L. G., and Montalvo-Arrieta, J. C.: Regional  
609 landslide hazard assessment from seismically induced displacements in Monterrey  
610 Metropolitan area, Northeastern Mexico, *Bull Eng Geol Environ*, 78, 1127–1141,  
611 <https://doi.org/10.1007/s10064-017-1087-3>, 2019.

612 Sassa, K., Nagai, O., Solidum, R., Yamazaki, Y., and Ohta, H.: An integrated model  
613 simulating the initiation and motion of earthquake and rain induced rapid landslides  
614 and its application to the 2006 Leyte landslide, *Landslides*, 7, 219–236,  
615 <https://doi.org/10.1007/s10346-010-0230-z>, 2010.

616 Sepúlveda, S. A., Murphy, W., Jibson, R. W., and Petley, D. N.: Seismically induced  
617 rock slope failures resulting from topographic amplification of strong ground motions:  
618 The case of Pacoima Canyon, California, *Engineering geology*, 80, 336–348, 2005.

619 Shukha, R. and Baker, R.: Design implications of the vertical pseudo-static coefficient

---

620 in slope analysis, *Computers and Geotechnics*, 35, 86–96, 2008.

621 Spencer, E.: A Method of analysis of the Stability of Embankments Assuming Parallel  
622 Inter-Slice Forces, *Géotechnique*, 17, 11–26, <https://doi.org/10.1680/geot.1967.17.1.11>,  
623 1967.

624 Sun, G., Cheng, S., Jiang, W., and Zheng, H.: A global procedure for stability analysis  
625 of slopes based on the Morgenstern-Price assumption and its applications, *Computers  
626 and Geotechnics*, 80, 97–106, 2016a.

627 Sun, G., Zheng, H., Huang, Y., and Li, C.: Parameter inversion and deformation  
628 mechanism of Sanmendong landslide in the Three Gorges Reservoir region under the  
629 combined effect of reservoir water level fluctuation and rainfall, *Engineering Geology*,  
630 205, 133–145, 2016b.

631 Sun, G., Yang, Y., Jiang, W., and Zheng, H.: Effects of an increase in reservoir  
632 drawdown rate on bank slope stability: a case study at the Three Gorges Reservoir,  
633 China, *Engineering Geology*, 221, 61–69, 2017.

634 Wang, H.-L. and Xu, W.-Y.: 3 D dynamical response analysis of high rock slope related  
635 to hydropower project in high intensive seismic region., *Yanshilixue Yu Gongcheng  
636 Xuebao/Chinese Journal of Rock Mechanics and Engineering*, 24, 5890–5895, 2005.

637 Yin, K.-L., Liu, Y.-L., Wang, Y., and Jiang, Z.-B.: Physical model experiments of  
638 landslide-induced surge in Three Gorges Reservoir, *Earth Science/Diqiu Kexue*, 37,  
639 2012.

640 Zhang, X.: Three-Dimensional Stability Analysis of Concave Slopes in Plan View, J.

---

641 Geotech. Engrg., 114, 658–671, [https://doi.org/10.1061/\(ASCE\)0733-](https://doi.org/10.1061/(ASCE)0733-)  
642 9410(1988)114:6(658), 1988.

643 Zheng, H.: A rigorous three-dimensional limit equilibrium method, Chinese Journal of  
644 Rock Mechanics and Engineering, 26, 1529–1537, 2007.

645 Zheng, H.: Eigenvalue Problem from the Stability Analysis of Slopes, J. Geotech.  
646 Geoenviron. Eng., 135, 647–656, [https://doi.org/10.1061/\(ASCE\)GT.1943-](https://doi.org/10.1061/(ASCE)GT.1943-)  
647 5606.0000071, 2009.

648 Zheng, Y., Shi, W. M., and Kong, W. X.: Calculation of seepage forces and phreatic  
649 surface under drawdown conditions, Chinese Journal of Rock Mechanics and  
650 Engineering, 23, 3203–3210, 2004.

651 Zhou, J. and Qin, C.: Stability analysis of unsaturated soil slopes under reservoir  
652 drawdown and rainfall conditions: Steady and transient state analysis, Computers and  
653 Geotechnics, 142, 104541, 2022.

654 Zhou, J., Chen, Q., and Wang, J.: Rigid block based lower bound limit analysis method  
655 for stability analysis of fractured rock mass considering rock bridge effects, Computers  
656 and Geotechnics, 86, 173–180, <https://doi.org/10.1016/j.compgeo.2017.01.016>, 2017.

657